Optimizing the resistivity of colloidal SnO_2 thin films by ion implantation and annealing

Abubakar Sadiq Yusuf[1,2,3], Martin Markwitz[2,4,5], Zhan Chen[1], Maziar Ramezani[1], John V. Kennedy[2,5], Holger Fiedler[2]

[1]School of Engineering, Computer and Mathematical Sciences, Auckland University of Technology, PO Box 92006, Auckland 1142, New Zealand

[2]National Isotope Centre, GNS Science, PO Box 30368, Lower Hutt 5010, New Zealand

[3]School of Physical Sciences, Department of Physics, Federal University of Technology, PMB 65, Minna, Niger State, Nigeria

[4]School of Chemical and Physical Sciences, Victoria University of Wellington, PO Box 600, Wellington 6140, New Zealand

[5]The MacDiarmid Institute for Advanced Materials and Nanotechnology, Victoria University of Wellington, PO Box 600, Wellington 6140, New Zealand

Abstract: Tin oxide (SnO_2) is a critical material for a wide range of applications, such as in perovskite solar cells, gas sensors as well as for photocatalysis. For these applications the transparency to visible light, high availability, cheap fabrication process and high conductivity of SnO_2 benefits commercial deployment. In this paper, we demonstrate that the resistivity of widely colloidal SnO_2 can be reduced by noble gas ion beam modification. After low energy implantation with a fluence of 4×10^{15} at.cm^{-2} at 25 keV and annealing 200˚C in open air, the resistivity of as-deposited film was (178.2 ± 6.1) μΩcm reduced to (133.2 ± 5.2) μΩcm, a reduction of 25 %. Hall effect measurements showed that the primary cause of this is the increase in carrier concentration from $(8.1 \pm 0.3) \times 10^{20}$ cm^{-3} to $(9.9 \pm 0.3) \times 10^{20}$ cm^{-3}. Annealing at 200˚C resulted in the removal of defect clusters introduced by implantation, while annealing at 300˚C resulted in the oxidation of the films, increasing their resistivity. The concentration of oxygen vacancy defects can be controlled by a combination of low energy noble gas ion implantation and annealing, providing promising performance increases for potential applications of SnO_2 where a low resistivity is crucial.

Keywords

Tin oxide; argon; implantation; annealing; resistivity

1. Introduction

Since their inception in 2009 perovskite solar cells have shown a tremendous increase in power conversion efficiency (PCE) and stability. In 2024, the verified record efficiency of a single-junction perovskite solar cell has been 25.8 %, exceeding for the first time the efficiency of state-of-the-art Si solar cells. Both technologies can be combined and the efficiency of a perovskite-silicon tandem solar cell of 33.7 % has been reported [1,2].

This rapid increase in perovskite solar cell efficiency is largely enabled by suitable charge transport layers for electrons (ETL) and holes (HTL), which must match the conduction and valence band energies of the perovskite absorber layer, respectively [3,4]. The dominant characteristic of a charge carrier layer is the high conduction of the majority charge carrier and the blocking of the minority charge carrier to suppress carrier recombination and thus maximise the short-circuit current [5,6]. For an inverted solar cell architecture, high transparency of the HTL is critical, while in normal architecture, the ETL must possess high optical transmittance [1].

Typical HTLs are the organics 2,2',7,7'-tetrakis(N,N-di-p-methoxyphenylamine)-9,9'-spirobifluorene (spiro-OMeTAD) [7], PEDOT:PSS [8] and inorganic layers such as NiO [9] or CuI [8], while classical ETLs layers are SnO_2 [10,11] TiO_2 [12] and ZnO [13], with colloidal SnO_2 currently the commercially most promising and cost-efficient material if scalable technologies such as spin coating [11] and chemical bath deposition (CBD) [14] are employed. For perovskite solar cells SnO_2 is today considered one of the most promising ETLs, but colloidal SnO_2 is also a useful material for gas sensors, for which low resistivity SnO_2 and high conductivity are critical material properties [15].

We previously have shown that both ZnO, In_2O_3, and CuI ion implantation can tune the conductivity of transparent conducting thin films by chemical doping and the introduction of point defects [16-18]. Previous research has demonstrated the impact of implant-induced damage on the electrical properties of Sn-doped In_2O_3 (ITO) films on SiO_2-coated soda-lime glass substrates, indicating that implantation can significantly alter the electrical properties of transparent conducting oxides through the introduction of structural damage and defects [19] [20,21]. Depending on the compound, the defects introduced by ion implantation can act as carrier traps; reducing mobility or be beneficial for the conductivity by introducing additional donor/acceptor states, increasing the carrier concentration. In ScN, for example, annealing restores crystallinity, which is beneficial by improving the films' electrical properties [22].

In this work, we study the impact of noble gas (argon) ion implantation on the electrical and optical properties of a SnO_2 nanoparticle thin film and demonstrate the implantation and annealing conditions required to reduce the resistivity of colloidal SnO_2 thin films, themselves prepared through spin coating.

2. Material and Methods

Tin oxide colloidal nanoparticles (colloidal dispersion 15 wt.% in water) were purchased from Alfa Aesar. Tin oxide thin films were deposited onto 10 × 10 mm^2 soda-lime microscope glass and Si(001) substrates. The substrates were ultrasonically cleaned in acetone, followed by ethanol, then deionised water, for 10 minutes each after which substrates were treated with UV Ozone at 50˚C for 30 minutes to remove any organic contaminants. 100 μL of the SnO_2 suspension was pipette onto the centre of the substrate before starting the spin coating program. Spin coating was performed at 2000 rpm for 30 seconds to deposit 90 nm colloidal SnO_2 thin films. Subsequently, the films were annealed on a hotplate at 100˚C for 60 min.

To optimize for an implantation damage profile within the SnO_2 thin film the implantation energy was determined through Monte Carlo simulation with T-DYN [23]. For the simulations, a density of the SnO_2 film of 6.95 g/cm^3 and a thickness of 100 nm was assumed. Argon was implanted with an acceleration energy of 25 keV for a fluence of 1×10^{15}, 2×10^{15}, 4×10^{15} and 6×10^{15} Ar cm^{-2}. A scanner was used to achieve homogeneous implantation of the 1 × 1 cm^2 films with a current density of 3.6 μAcm^{-2} [24]. After implantation, a selection of films were annealed in open air using a hot plate for at 200˚C and 300˚C for 60 minutes.

Characterization

Transmittance spectra were measured with a (PerkinElmer Lamba 365) UV-Visible spectrophotometer using 0.5 nm spectral bandwidth (SBW), data interval 0.5 nm and scan rate 300 (nm/min). The colloidal SnO_2 film thicknesses of each series of samples were measured using Rutherford backscattering spectrometry (RBS) with the detector at 165° relative to the incident 2.0 MeV $^4He^+$ beam to a charge of 20 μC [25,26]. The data acquired through the RBS measurement were analyzed with SIMNRA [27]. Silver paste contacts were applied onto the corners of the SnO_2 films for resistivity and Hall effect measurements, conducted with the Ecopia HMS-3000 equipment using the van der Pauw contact geometry and a 0.55 T magnetic field. The films' structural properties were investigated with grazing-incidence x-ray diffraction (GIXRD) using a Rigaku SmartLab x-ray diffractometer with a Cu x-ray source (K

α_1 λ = 1.540 Å, K α_2 λ = 1.544 Å). A grazing incidence angle of $\omega = 1.5^{\circ}$ was used for this measurement.

3. Results

The concentration profile of Ar^+ in each of these samples was calculated by the T-DYN Monte Carlo simulation package for the fluences 1, 2, 4 and 6×10^{15} at.cm^{-2}, as shown in Figure 1. Figure 1 shows the ion implantation results in a Gaussian-like distribution of implanted ions, as demonstrated by the Ar concentration profile. For the samples prepared by implanting Ar^+ ions into a SnO_2 film at 25 keV to a highest fluence of 6×10^{15} at.cm^{-2} a maximum Ar concentration of 3 at. % at a depth of ~48.4 nm (mean projected range) is predicted.

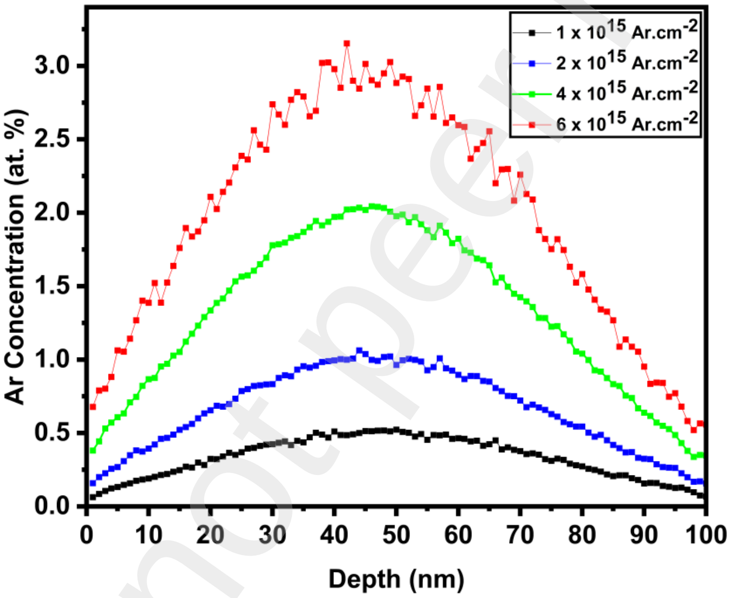

Figure 1. (Color online) T-DYN Monte Carlo simulation of the Ar concentration as a function of depth for samples (1×10^{15} at.cm^{-2}, 2×10^{15} at.cm^{-2}, 4×10^{15} at.cm^{-2}, 6×10^{15} at.cm^{-2} Ar; 25 keV).

UV–VIS transmittance spectra were collected for as-deposited, 6×10^{15} at.cm^{-2} Ar^+, 6×10^{15} at.cm^{-2} Ar^+ and annealing at 200˚C and 6×10^{15} at.cm^{-2} Ar^+ and annealing at 300˚C to estimate the visible transmittance in Figure 2. Figure 2 shows the transmittance as a function of wavelength over the visible range. The optical transparency of the films is measured relative to the substrate, decreasing from 76 ± 9 % in (SnO_2) as-deposited films to 70 ± 9 % after implantation with a fluence of 6 x 10^{15} Ar.cm^{-2} film. Transparency was recovered to 75 ± 2 % and 77 ± 1 % after annealing at 200˚C and 300˚C, respectively.

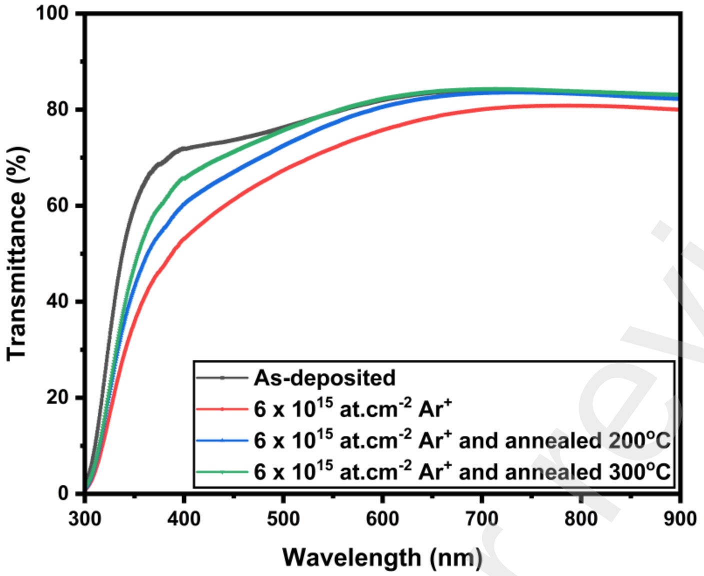

Figure 2. (Color online) UV-Vis transmittance of as-deposited (black), 6 × 10^{15} at.cm^{-2} Ar^+ as-implanted sample (red), in addition to the equivalently implanted samples annealed at 200˚C (blue) and 300˚C (green).

RBS and XRD measurements were done to investigate variations in the structural and compositional properties of the argon-implanted spin coated SnO_2 colloidal films. In particular, the composition, film thickness, and phase purity were studied.

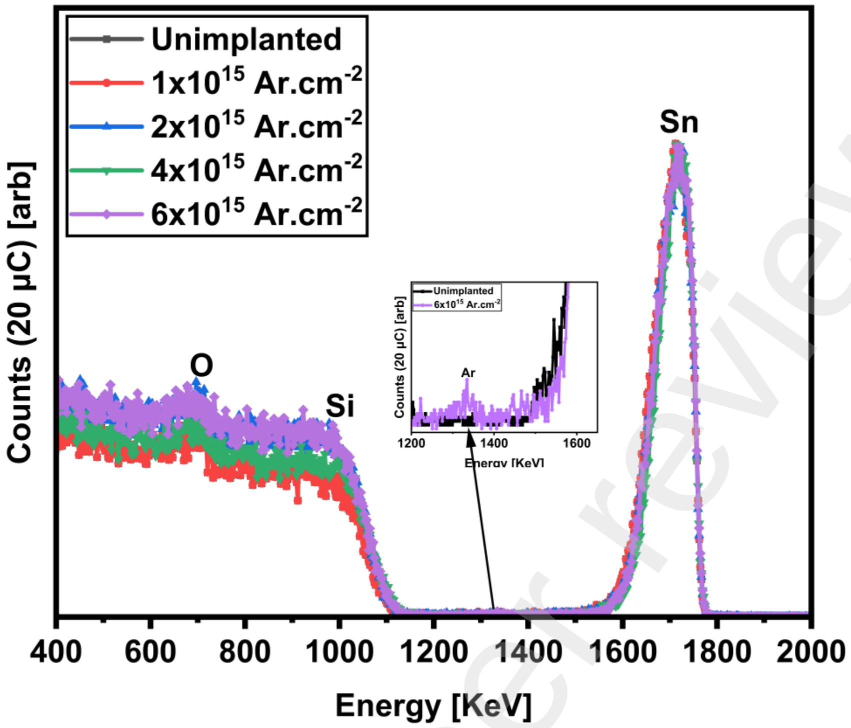

Figure 3. (Color online) 2.0 MeV $^4He^+$ RBS of the argon implanted SnO_2 colloidal thin films deposited on silicon. The inset highlights the incorporation of Ar for the highest investigated fluence.

Figure 3 shows the backscattering spectra of the implanted argon into tin oxide deposited on a silicon substrate, confirming that the deposited SnO_2 colloidal films are free from high atomic number impurities. An inset graph demonstrates the presence of argon in the most-implanted sample. Analysis with SIMNRA finds that the SnO_2 films are stoichiometric with a ratio of Sn:O of 1:2, in good agreement with the results within reference [28]. The thicknesses of the deposited, implanted, and annealed films were ranging between 87 and 93 nm, suggesting a high degree of reproducibility for the spin coating process.

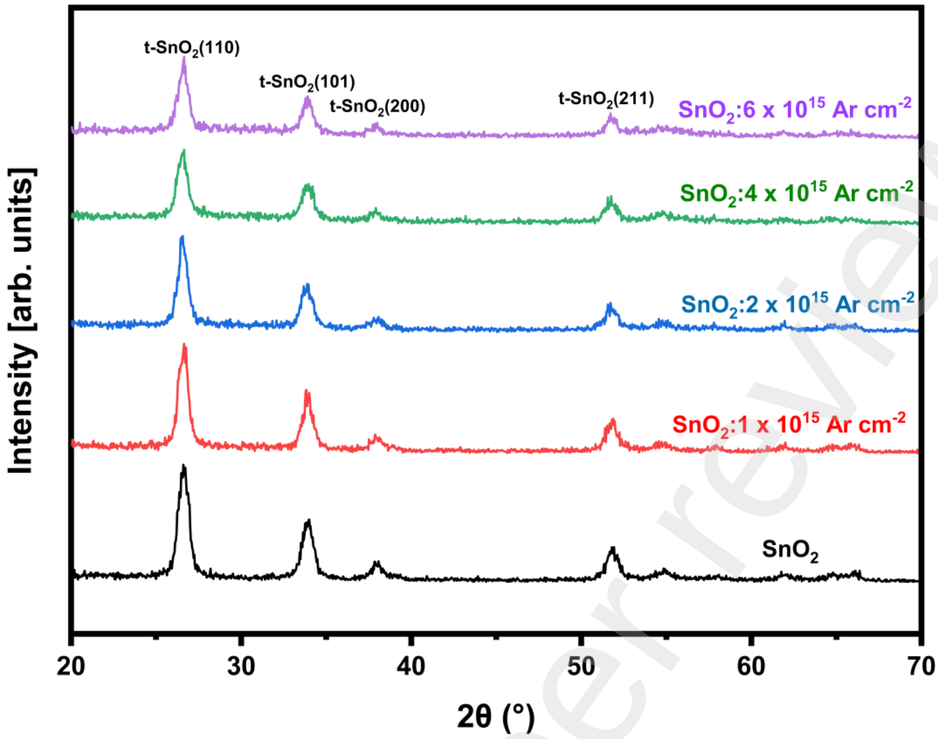

Figure 4. GIXRD patterns of the SnO_2 film deposited on a Silicon substrate after Ar^+ implantation.

Figure 4 shows the GIXRD pattern of the SnO_2 film deposited on a silicon substrate as a function of implantation fluence. The diffraction patterns show SnO_2 peaks at (110), (101), (200) and (211) at 2θ diffraction angles 26.61°, 33.90°, 38.01° and, 51.81°, respectively, whilst no other peaks were detected indicating the absence of impurity phases within the XRD detection limit. The XRD pattern finds that the spin-coated SnO_2 films are polycrystalline, and these peaks belong to the cassiterite crystal phase with a tetragonal rutile structure (JCPDS No. 01-090-6586). Using Bragg's law

$$\lambda = 2d_{hkl}\sin\theta \qquad (1)$$

with $\lambda = 1.54059$ Å (Cu K α_1 x-ray wavelength) and d_{hkl} the appropriate lattice plane. The lattice constants associated with the (200) peak positions were calculated by fitting split pseudo-Voigt functions to the peaks in the measured GIXRD patterns, the fitting conducted with the Rigaku SmartLabs Studio II software. The crystallite size (D) of the films was estimated using the Debye-Scherrer formula given as

$$D = K\lambda/\beta\cos\theta\,, \qquad (2)$$

where K = 0.94 is the spherical nanoparticle shape factor [29], λ is the x-ray wavelength, β is the full width at half maximum of the (110) peak in radians, and θ is the Bragg angle in radians. The derived FWHM of pristine SnO$_2$ doesn't significantly vary for the deposited and implanted films, both before and after annealing, suggesting that the overall grain morphology remains unchanged. Prior to implantation and annealing the SnO$_2$ film has a lattice constant of 4.73 ± 0.01 Å, remaining unchanged after implantation with the highest fluence of 6×10^{15} at.cm^{-2}, both before and after annealing. The as-deposited SnO$_2$ has a lattice constant c of 3.18 ± 0.01 Å, which also does not significantly vary upon implantation and annealing, suggesting an overall negligible effect on the overall crystal structure. The lattice parameters, full width at half maximum (FWHM), and average crystallite sizes of the colloidal SnO$_2$ are provided in Table S1 and S2 and Figure S2 (a-d) for both non-annealed and annealed samples.

Table 1.

Room temperature hall effect measurement properties of colloidal SnO$_2$ films both implanted and unannealed and implanted and annealed at 200˚C and 300˚C, respectively.

Fluence [$\times10^{15}$ Ar cm^{-2}]	Ar conc. [$\times10^{20}$ cm^{-3}]	Annealed	$\lvert\mu\rvert$ [cm^{2}V^{-1}s^{-1}]	$\lvert n\rvert$ [$\times10^{20}$ cm^{-3}]	ρ [$\mu\Omega$cm]
0	0	No	43.0±1.6	8.1±0.3	178.2±6.1
1×10^{15}	1	No	40.0±1.5	6.9±0.3	224.9±7.5
2×10^{15}	2	No	41.3±1.5	5.7±0.2	264.0±8.9
4×10^{15}	4	No	38.5±1.4	6.2±0.2	263.7±8.9
6×10^{15}	6	No	39.4±1.4	6.1±0.2	258.4±8.7
0	0	200˚C	47.8±1.4	8.3±0.4	158.2±5.5
1×10^{15}	1	200˚C	48.8±1.3	8.6±0.3	148.0±4.9
2×10^{15}	2	200˚C	48.8±1.3	9.6±0.3	134.8±4.9
4×10^{15}	4	200˚C	48.7±1.5	9.6±0.5	133.2±5.2
6×10^{15}	6	200˚C	47.1±1.4	9.9±0.3	134.5±4.5
0	0	300˚C	46.0±1.8	8.1±0.3	168.2±5.8
1×10^{15}	1	300˚C	46.5±1.7	5.4±0.2	250.8±8.6
2×10^{15}	2	300˚C	45.0±1.6	5.2±0.3	266.5±9.4
4×10^{15}	4	300˚C	47.0±1.5	4.8±0.2	275.1±9.7
6×10^{15}	6	300˚C	47.0±1.7	4.6±0.3	288.8±10.1

Based on the observed phase purity and the unchanged film composition, whilst the optical properties remarkably changed, we carried out four-point resistivity (ρ) measurements. Table I displays the fluence and concentration of argon which varies based on the implantation fluence as determined by T-DYN. While argon itself is not a dopant, the high concentration of defects it creates during the collision process are interpreted to lead to a modified conductivity. The expression used to calculate the carrier concentration is $n=(qR_H)^{-1}$, where q represents the elementary charge and R_H is the Hall coefficient. All samples exhibited a negative Hall coefficient, suggesting that the films maintain their n-type carrier charge. The Hall carrier mobility was calculated from $\mu=R_H/\rho$. The Hall factor was assumed to be unitary due to the high carrier concentrations measured for these samples. After implantation with the lowest fluence (1×10^{15} Ar cm^{-2}) there was a significant initial reduction in carrier concentration and mobility. The initial values of the carrier concentration and mobility were $(8.1 \pm 0.3) \times 10^{20}$ cm^{-3} and (43.0 ± 1.6) $cm^2V^{-1}s^{-1}$, decreasing to $(6.9 \pm 0.3) \times 10^{20}$ cm^{-3} and (40.0 ± 1.5) $cm^2V^{-1}s^{-1}$, respectively. The calculated results from the Hall effect measurements are shown in Table 1 and are also graphically represented in supplementary information in Figure S3. The initial reduction of both has been previously attributed to the formation of interstitial type defect clusters and so-called argon-vacancy complexes [22]. Beyond this initial drop in mobility, the mobility was only slightly further reduced upon further implantation, attributed to those specific defects inducing acceptor-type deep levels within the band gap. A final carrier mobility value of (38.5 ± 1.4) $cm^2V^{-1}s^{-1}$ was measured upon implantation with a fluence of 4×10^{15} Ar cm^{-2}. The decrease in carrier concentration is proportional to the concentration of implanted argon, indicating that argon implantation induces acceptor states. The first substantial decrease in carrier concentration is ascribed to the formation of defect clusters. These changes in carrier concentration and mobility directly impact the film resistivities. As resistivity is inversely proportional to the product of carrier concentration and mobility through $\rho=(nq\mu)^{-1}$, the observed decreases in both carrier concentration and mobility lead to a notable increase in resistivity. The initial value of the resistivity was (178.2 ± 6.1) μΩcm, which increased to (264.0 ± 8.9) μΩcm after implantation for fluence 2×10^{15} Ar cm^{-2}. The observed resistivity variations can be attributed to the evolution of specific defects induced by Argon implantation, which functions primarily as a source of acceptor-type deep levels.

Upon annealing in an open air at 200˚C, a partial recrystallization occurs, leading to the annihilation (or reduction in the concentration) of some of the detrimental acceptor-type defects. This process diminishes the density of electron traps, consequently enhancing the free carrier concentration and mobility, and thus lowering the resistivity to (133.2 ± 5.2) μΩcm for fluence 4×10^{15} Ar cm^{-2} [30]. Crucially, the donor defects, hypothesized to be oxygen vacancies V_O introduced by the implantation are not annealed out, maintaining their beneficial properties.

However, elevating the annealing temperature to 300˚C initiates a more complex defect evolution mechanism. At this elevated temperature, the acceptor-type deep levels may undergo transformation into more thermodynamically stable extended defects or coalesce into clusters. These modifications substantially increase both the concentration and efficiency of acceptor-type deep levels, resulting in enhanced electron trapping and consequently, higher resistivity compared to the 200˚C annealing stage [31].

Our results suggest that the transmittance reduction is directly linked to a reduction in carrier mobility, which depends sensitively on the films' nanostructure, modified by sequential ion implantation and annealing. Argon ion implantation causes the formation of stable defects, such as interstitial-type defect clusters and argon vacancy complexes, which can be selectively evolved by a post-implantation temperature treatment. Ion implantation with a subsequent mild temperature (200˚C) annealing procedure, simultaneously eliminates detrimental defects (defect clusters) while retaining the beneficial vacancy defects. In contrast, annealing at higher temperatures (300˚C) may lead to the evolution of the detrimental defects and the removal of the beneficial defects.

4. Conclusion

In this paper, we have demonstrated that the resistivity of colloidal spin-coated SnO_2 can be reduced by Ar^+ ion implantation from (264.0 ± 8.9) μΩcm to (133.2 ± 5.2) μΩcm after subsequent annealing at 200˚C in the open air. The implantation provides a combination of beneficial and detrimental defects, the detrimental defects can be annealed out at 200˚C, revealing increased performance, while annealing at 200˚C also removes the beneficial defects. The interplay between the ion beam induced damage and selective defect engineering by annealing temperature control could provide tremendously in developing scalable methods for control-modification of SnO_2 colloidal thin films. This low-temperature process is useful for use in ETL's, whereby a reduced resistivity by an increased carrier concentration may be useful for thin film ETL fabrication for improved perovskite-based solar cell performance.

Acknowledgement

The authors would like to acknowledge C. Purcell (National Isotope Centre, GNS Science, New Zealand) for conducting the RBS measurements. ASY would like to thank the Tertiary Education Trust Fund (Tetfund) for funding TETF/ES/UNIV/NIGER STATE/TSAS/2020. This project was partly funded by the Royal Society of New Zealand under Marsden contract

MFP-GNS2202 and by the New Zealand Ministry for Business, Innovation and Employment through the Materials for Low Carbon Future Program (C05X1702).

Declaration of Competing Interest

The authors declare that they have no known competing financial interests or personal relationships that could have influenced the work reported in this study.

Data Availability

Data will be made available on request.

References

[1] Afre, R.A. and D. Pugliese, *Perovskite Solar Cells: A Review of the Latest Advances in Materials, Fabrication Techniques, and Stability Enhancement Strategies.* Micromachines (Basel), 2024. **15**(2). DOI: 10.3390/mi15020192.

[2] Lim, J., N.-G. Park, S.I. Seok, and M. Saliba, *All-perovskite tandem solar cells from fundamentals to technological progress.* Energy & Environmental Science, 2024. DOI: 10.1039/D3EE03638C.

[3] Subudhi, P. and D. Punetha, *Pivotal avenue for hybrid electron transport layer-based perovskite solar cells with improved efficiency.* Scientific Reports, 2023. **13**(1): p. 19485. DOI: 10.1038/s41598-023-33419-1.

[4] Gu, Y.-F., H.-J. Du, N.-N. Li, L. Yang, and C.-Y. Zhou, *Effect of carrier mobility on performance of perovskite solar cells*.* Chinese Physics B, 2019. **28**(4): p. 048802. DOI: 10.1088/1674-1056/28/4/048802.

[5] Zhang, S., X. Jia, Q. Geng, Z. He, Y. Hu, Y. Gao, S. Yang, C. Yao, Q. Zhang, D. Wang, and Y. Wu, *Solvent engineering of SnO2 electron transport layer for high-performance perovskite solar cells.* Surfaces and Interfaces, 2023. **41**: p. 103226. DOI: https://doi.org/10.1016/j.surfin.2023.103226.

[6] Youn, S.S.-O., J. Kim, J. Na, W. Jo, and G.Y. Kim, *Understanding the Space-Charge Layer in SnO2 for Enhanced Electron Extraction in Hybrid Perovskite Solar Cells.* ACS Applied Materials & Interfaces, 2022. **14**(42): p. 48229-48239. DOI: 10.1021/acsami.2c12461.

[7] Malinkiewicz, O., A. Yella, Y.H. Lee, G.M. Espallargas, M. Graetzel, M.K. Nazeeruddin, and H.J. Bolink, *Perovskite solar cells employing organic charge-transport layers.* Nature Photonics, 2014. **8**(2): p. 128-132. DOI: 10.1038/nphoton.2013.341.

[8] Sun, W., S. Ye, H. Rao, Y. Li, Z. Liu, L. Xiao, Z. Chen, Z. Bian, and C. Huang, *Room-temperature and solution-processed copper iodide as the hole transport layer for inverted planar perovskite solar cells.* Nanoscale, 2016. **8**(35): p. 15954-15960. DOI: 10.1039/C6NR04288K.

[9] Kim, J.H., P.-W. Liang, S.T. Williams, N. Cho, C.-C. Chueh, M.S. Glaz, D.S. Ginger, and A.K.Y. Jen, *High-Performance and Environmentally Stable Planar Heterojunction Perovskite Solar Cells Based on a Solution-Processed Copper-Doped Nickel Oxide Hole-Transporting Layer.* Advanced Materials, 2015. **27**(4): p. 695-701. DOI: https://doi.org/10.1002/adma.201404189.

[10] Eliwi, A.A., M. Malekshahi Byranvand, P. Fassl, M.R. Khan, I.M. Hossain, M. Frericks, S. Ternes, T. Abzieher, J.A. Schwenzer, T. Mayer, J.P. Hofmann, B.S. Richards, U. Lemmer, M. Saliba, and U.W. Paetzold, *Optimization of SnO2 electron transport layer for efficient planar perovskite solar cells with very low hysteresis.* Materials Advances, 2022. **3**(1): p. 456-466. DOI: 10.1039/D1MA00585E.

[11] Song, K., X. Zou, H. Zhang, C. Zhang, J. Cheng, B. Liu, Y. Yao, X. Wang, X. Li, Y. Wang, and B. Ren *Effect of SnO2 Colloidal Dispersion Solution Concentration on the Quality of Perovskite Layer of Solar Cells*. Coatings, 2021. **11**, DOI: 10.3390/coatings11050591.

[12] Zhao, W., P. Guo, J. Wu, D. Lin, N. Jia, Z. Fang, C. Liu, Q. Ye, J. Zou, Y. Zhou, and H. Wang, *TiO2 Electron Transport Layer with p–n Homojunctions for Efficient and Stable Perovskite Solar Cells.* Nano-Micro Letters, 2024. **16**(1): p. 191. DOI: 10.1007/s40820-024-01407-3.

[13] Liu, C., C. Xiao, and W. Li, *Zinc oxide nanoparticles as electron transporting interlayer in organic solar cells.* Journal of Materials Chemistry C, 2021. **9**(40): p. 14093-14114. DOI: 10.1039/D1TC03434K.

[14] Tong, G., L.K. Ono, Y. Liu, H. Zhang, T. Bu, and Y. Qi, *Up-Scalable Fabrication of SnO2 with Multifunctional Interface for High Performance Perovskite Solar Modules.* Nano-Micro Letters, 2021. **13**(1): p. 155. DOI: 10.1007/s40820-021-00675-7.

[15] Gil, B., A.J. Yun, J. Lim, J. Cho, B. Kim, S. Ryu, J. Kim, and B. Park, *Design of SnO2 Electron Transport Layer in Perovskite Solar Cells to Achieve 2000 h Stability Under 1 Sun Illumination and 85 °C.* Advanced Materials Interfaces, 2023. **10**(11): p. 2202148. DOI: https://doi.org/10.1002/admi.202202148.

[16] Kennedy, J., P.P. Murmu, J. Leveneur, V.M. Williams, R.L. Moody, T. Maity, and S.V. Chong, *Enhanced power factor and increased conductivity of aluminum doped zinc oxide thin films for thermoelectric applications.* Journal of nanoscience and nanotechnology, 2018. **18**(2): p. 1384-1387.

[17] Markwitz, M., S.Y. Back, E.X.M. Trewick, P.P. Murmu, T. Mori, B.J. Ruck, and J.V. Kennedy, *Quasilinear Kane conduction band model in nitrogen-doped indium tin oxide.* Physical Review B, 2024. **109**(11): p. 115201. DOI: 10.1103/PhysRevB.109.115201.

[18] Markwitz, M., P.P. Murmu, S.Y. Back, T. Mori, J.V. Kennedy, and B.J. Ruck, *Fermi energy modulation by tellurium doping of thermoelectric copper(I) iodide.* Materials Today Physics, 2024. **46**: p. 101513. DOI: https://doi.org/10.1016/j.mtphys.2024.101513.

[19] Vink, T.J., M.H.F. Overwijk, and W. Walrave, *The active dopant concentration in ion implanted indium tin oxide thin films.* Journal of Applied Physics, 1996. **80**(7): p. 3734-3738. DOI: 10.1063/1.363324.

[20] Tao, Z., H. Junda, and L. Hong, *Modification of tin dioxide thin films by ion implantation.* Applied Surface Science, 2000. **161**(3): p. 459-464. DOI: https://doi.org/10.1016/S0169-4332(00)00359-7.

[21] Shigesato, Y., D.C. Paine, and T.E. Haynes, *Study of the effect of ion implantation on the electrical and microstructural properties of tin-doped indium oxide thin films.* Journal of Applied Physics, 1993. **73**(8): p. 3805-3811. DOI: 10.1063/1.352887.

[22] Burcea, R., J.-F. Barbot, P.-O. Renault, D. Eyidi, T. Girardeau, M. Marteau, F. Giovannelli, A. Zenji, J.-M. Rampnoux, S. Dilhaire, P. Eklund, and A. le Febvrier, *Influence of Generated Defects by Ar Implantation on the Thermoelectric Properties of ScN.* ACS Applied Energy Materials, 2022. **5**(9): p. 11025-11033. DOI: 10.1021/acsaem.2c01672.

[23] Biersack, J.P., S. Berg, and C. Nender, *T-DYN Monte Carlo simulations applied to ion assisted thin film processes.* Nuclear Instruments and Methods in Physics Research Section B: Beam Interactions with Materials and Atoms, 1991. **59-60**: p. 21-27. DOI: https://doi.org/10.1016/0168-583X(91)95167-C.

[24] Fiedler, H., F. Fuchs, J. Leveneur, M. Nancarrow, D.R.G. Mitchell, J. Schuster, and J. Kennedy, *Giant Piezoelectricity of Deformed Aluminum Nitride Stabilized through Noble Gas Interstitials for Energy Efficient Resonators.* Advanced Electronic Materials, 2021. **7**(8): p. 2100358. DOI: https://doi.org/10.1002/aelm.202100358.

[25] Kennedy, J., W.J. Trompetter, P. Murmu, J. Leveneur, P.G. Sridhar Gupta, H. Fiedler, F. Fang, J. Futter, and C. Purcell, *Evolution of Rutherford's ion beam science to applied research activities at GNS Science.* Journal of the Royal Society of New Zealand, 2021. **51**: p. 1-18. DOI: 10.1080/03036758.2021.1897021.

[26] Kennedy, J., A. Markwitz, H.J. Trodahl, B.J. Ruck, S.M. Durbin, and W. Gao, *Ion Beam Analysis of Amorphous and Nanocrystalline Group III-V Nitride and ZnO Thin Films.* Journal of Electronic Materials, 2007. **36**(4): p. 472-482. DOI: 10.1007/s11664-006-0051-y.

[27] Mayer, M., *SIMNRA user's guide.* 1997.

[28] Babalola, A.V., V. Oluwasusi, V.A. Owoeye, J.O. Emegha, D.A. Pelemo, A.Y. Fasasi, U.M. Gurku, S.O. Alayande, S. Yusuf, and B. Saje M, *Effect of tin concentrations on the elemental and optical properties of zinc oxide thin films.* Heliyon, 2024. **10**(1): p. e23190. DOI: https://doi.org/10.1016/j.heliyon.2023.e23190.

[29] Harrington, G.F. and J. Santiso, *Back-to-Basics tutorial: X-ray diffraction of thin films.* Journal of Electroceramics, 2021. **47**(4): p. 141-163. DOI: 10.1007/s10832-021-00263-6.

[30] Balk, P., M. Aslam, and D.R. Young, *High temperature annealing behavior of electron traps in thermal SiO2.* Solid-State Electronics, 1984. **27**(8): p. 709-719. DOI: https://doi.org/10.1016/0038-1101(84)90019-4.

[31] Burmistrova, P.V., J. Maassen, T. Favaloro, B. Saha, S. Salamat, Y. Rui Koh, M.S. Lundstrom, A. Shakouri, and T.D. Sands, *Thermoelectric properties of epitaxial ScN films deposited by reactive magnetron sputtering onto MgO(001) substrates.* Journal of Applied Physics, 2013. **113**(15): p. 153704. DOI: 10.1063/1.4801886.

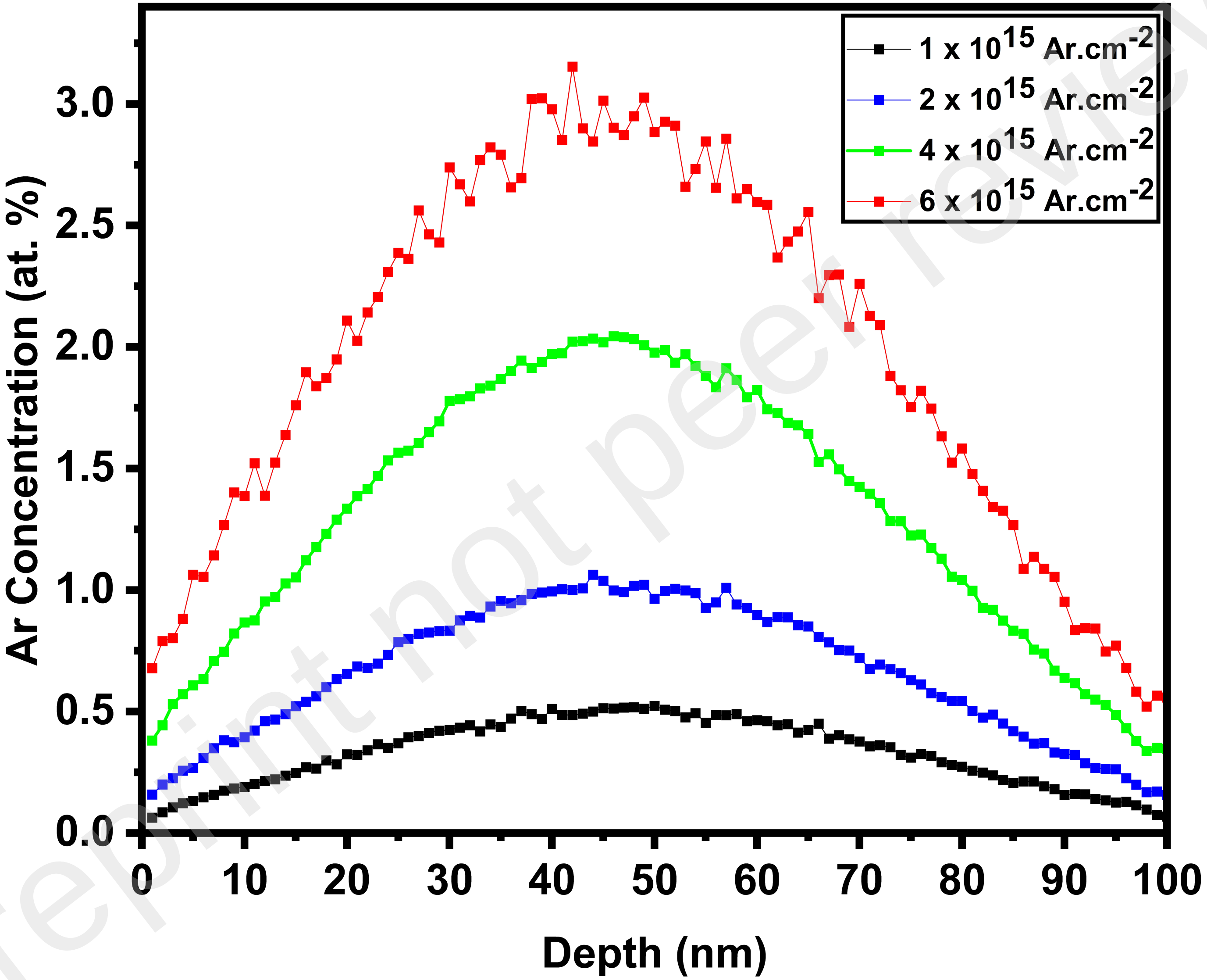
Ar Concentration (at. %)
0.0
0.5
1.0
1.5
2.0
2.5
3.0
Depth (nm)
0
10
20
30
40
50
60
70
80
90
100
1 x 10^15 Ar.cm^-2
2 x 10^15 Ar.cm^-2
4 x 10^15 Ar.cm^-2
6 x 10^15 Ar.cm^-2

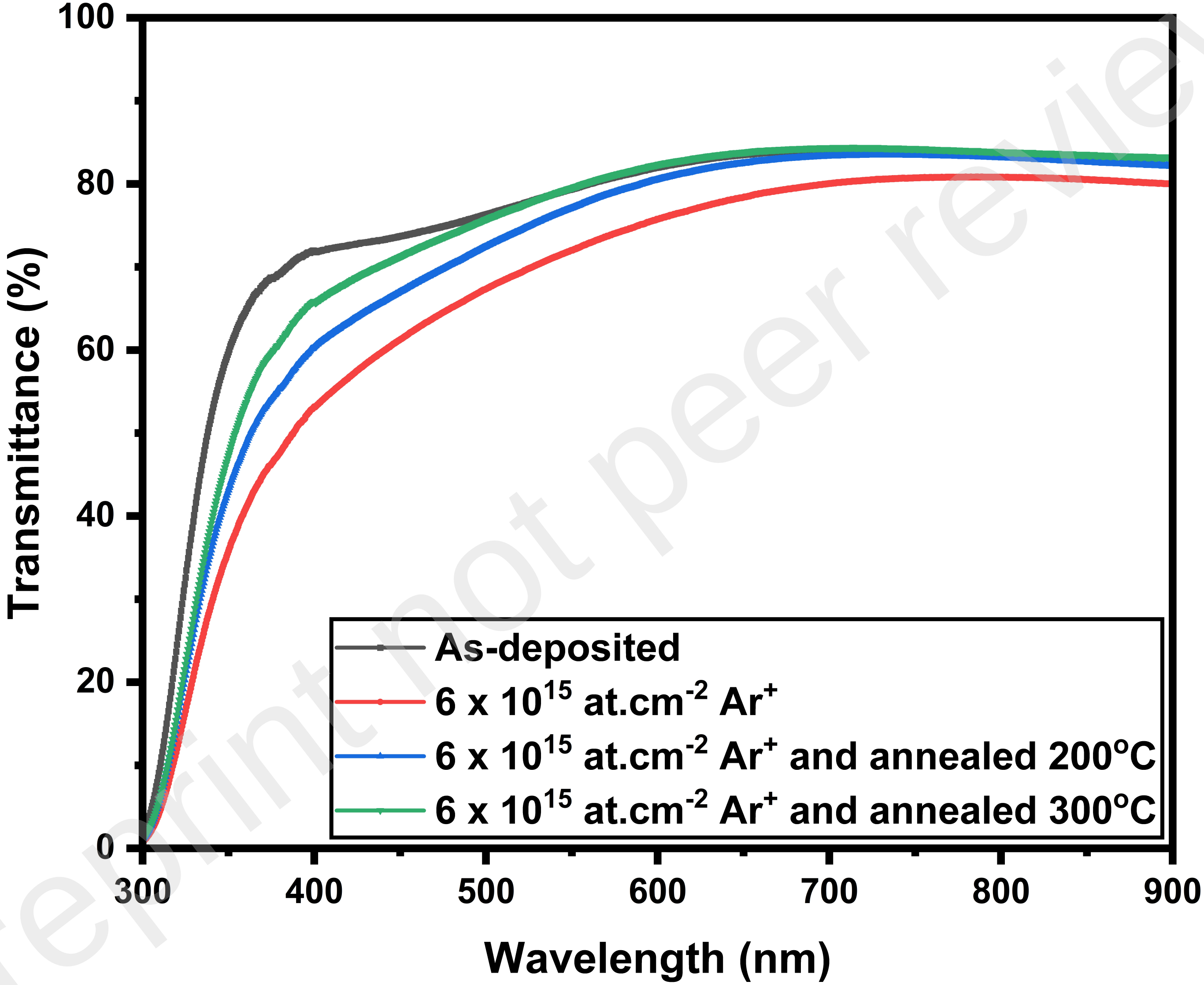
Transmittance (%)
100
80
60
40
20
0
300
400
500
600
700
800
900
Wavelength (nm)
As-deposited
6 x 10^{15} at.cm^{-2} Ar^{+}
6 x 10^{15} at.cm^{-2} Ar^{+} and annealed 200^{o}C
6 x 10^{15} at.cm^{-2} Ar^{+} and annealed 300^{o}C

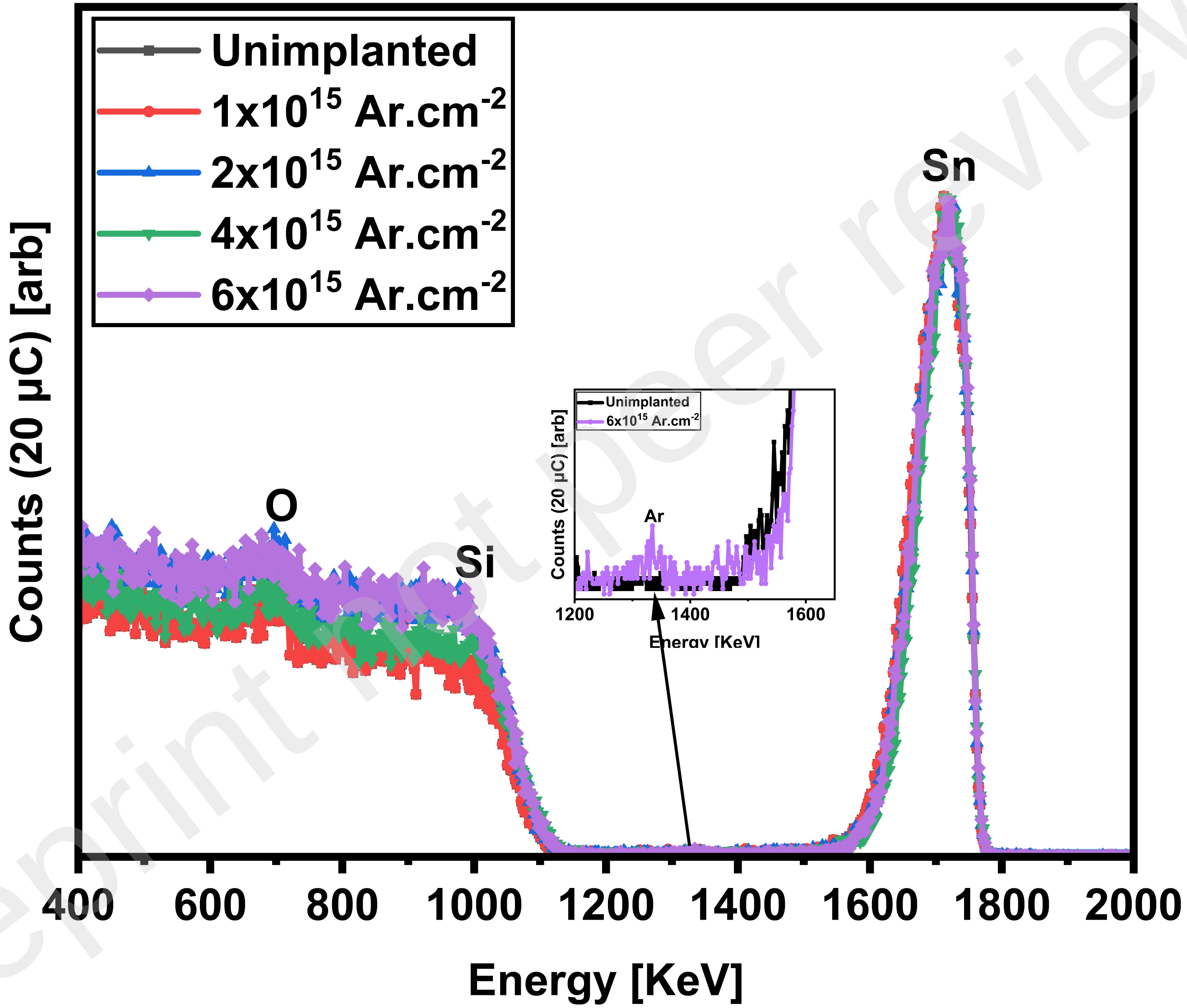
Unimplanted
1x10^15 Ar.cm^-2
2x10^15 Ar.cm^-2
4x10^15 Ar.cm^-2
6x10^15 Ar.cm^-2
Sn
O
Si
Ar
Unimplanted
6x10^15 Ar.cm^-2
Counts (20 µC) [arb]
1200
1400
1600
Energy [KeV]
Counts (20 µC) [arb]
400
600
800
1000
1200
1400
1600
1800
2000
Energy [KeV]

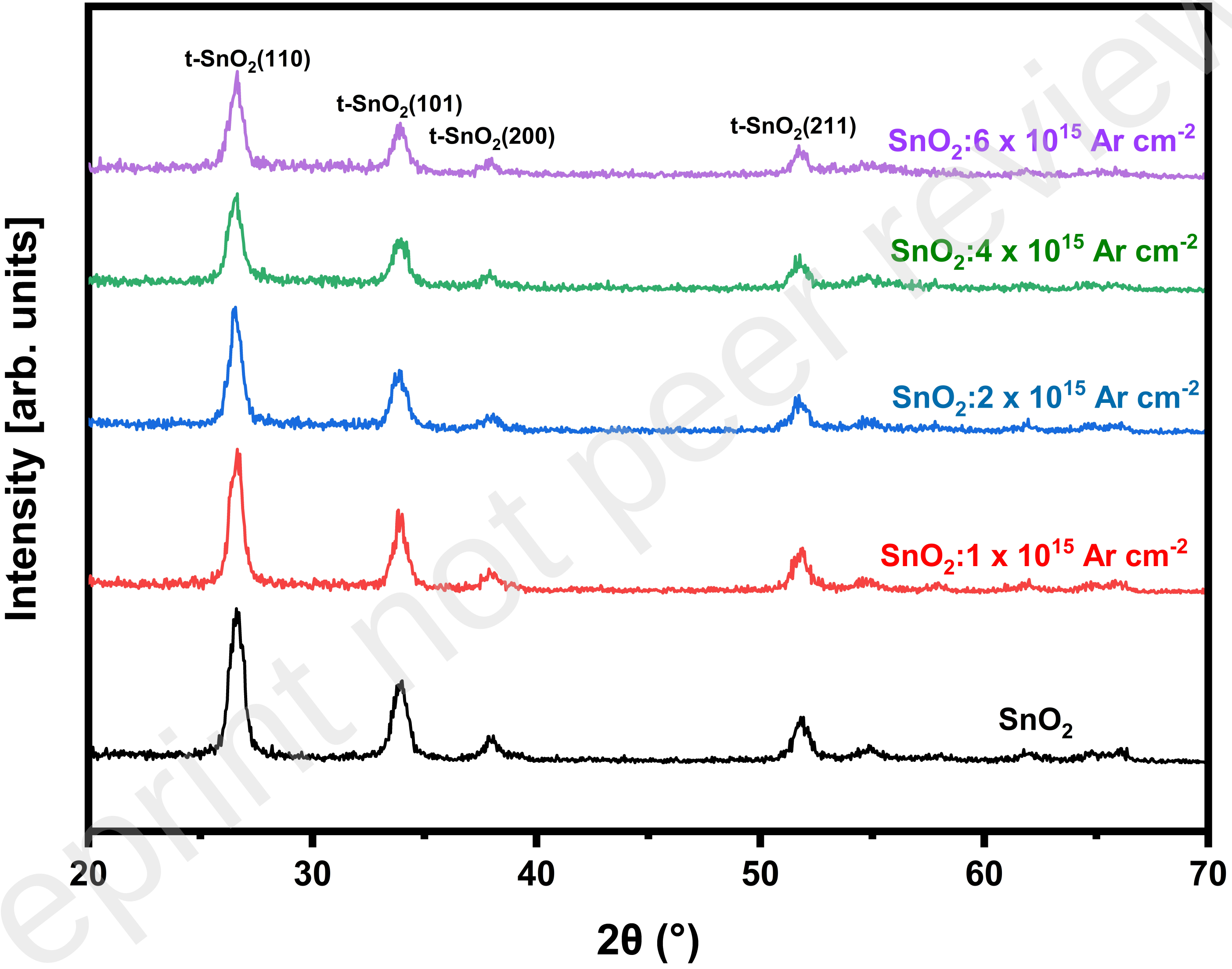
t-SnO$_2$(110)
t-SnO$_2$(101)
t-SnO$_2$(200)
t-SnO$_2$(211)
SnO$_2$:6 x 10^{15} Ar cm^{-2}
SnO$_2$:4 x 10^{15} Ar cm^{-2}
SnO$_2$:2 x 10^{15} Ar cm^{-2}
SnO$_2$:1 x 10^{15} Ar cm^{-2}
SnO$_2$
Intensity [arb. units]
20
30
40
50
60
70
2θ (°)